ACS APPLIED MATERIALS & INTERFACES

Research Article

Cite This: ACS Appl. Mater. Interfaces 2020, 12, 953−962

www.acsami.org

# Nonaqueous Polymer Combustion Synthesis of Cubic $Li_7La_3Zr_2O_{12}$ Nanopowders

J. Mark Weller, Justin A. Whetten, and Candace K. Chan*

Materials Science and Engineering, School for Engineering of Matter, Transport and Energy, Arizona State University, Tempe, Arizona 85287-6106, United States

Supporting Information

**ABSTRACT:** Garnet-type lithium lanthanum zirconate ($Li_7La_3Zr_2O_{12}$, LLZO) shows great promise as a solid electrolyte for future solid-state lithium batteries as it possesses a uniquely beneficial combination of high ionic conductivity, electrochemical stability against metallic lithium, and generally low reactivity in ambient conditions. Conventionally synthesized by using solid-state reactions, LLZO powders have also been prepared by using variations of sol−gel or combustion synthesis with sacrificial organic templates or polymers containing metal nitrate precursors. Herein, a novel nonaqueous polymer (NAP) method using metal-organic precursors and poly(vinylpyrrolidone) is demonstrated to easily form LLZO nanopowders. Compared to similar techniques using aqueous solutions with metal nitrates, the NAP method confers greater control over synthesis conditions. Undoped cubic phase LLZO is obtained after calcination at 700−800 °C between 0 and 4 h, and the NAP process is easily extended to Ta-doped LLZO. To elucidate the general formation mechanism of nanosized LLZO in the NAP combustion synthesis, scanning transmission electron microscopy is used to perform energy dispersive X-ray and electron energy loss spectral imaging. The results show that *in situ* formation of a carbonaceous foam during combustion physically segregates pockets of reagents and is responsible for maintaining the small particle size of the as-synthesized material during combustion and crystallization. The room temperature ionic conductivity of nanosized Ta-doped LLZO synthesized by using the NAP method was studied under various sintering conditions, with ionic conductivities between 0.24 and 0.67 mS $cm^{-1}$, activation energies between 0.34 and 0.42 eV, and relative densities in excess of 90% obtained by sintering at 1100 °C for between 6 and 15 h.

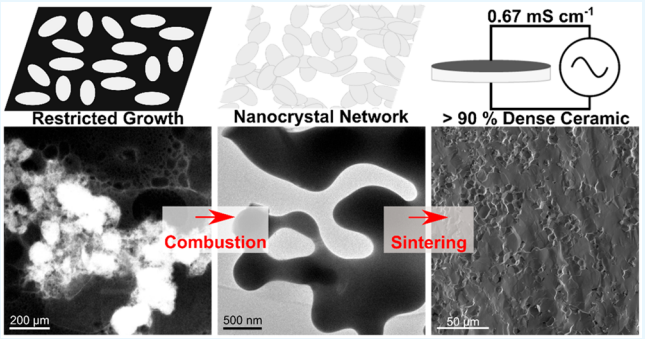


**KEYWORDS:** *solid electrolyte, lithium ion conductor, nanoparticle, combustion synthesis, garnet, $Li_7La_3Zr_2O_{12}$, sintering, LLZO*

## INTRODUCTION

Garnet-structured lithium lanthanum zirconate ($Li_7La_3Zr_2O_{12}$, LLZO) is a promising Li-ion conductor that has received much interest as a ceramic electrolyte for solid-state lithium batteries due to its high ionic conductivity and electrochemical stability against lithium metal.[1−3] LLZO is conventionally synthesized via solid-state reaction (SSR), which requires high temperatures (often ≥900 °C) and long calcination times (often >8−12 h) to obtain the desired cubic phase.[3] The high energy cost of conventional SSR has motivated numerous researchers to develop alternative lower temperature synthesis methods.[4−11] In general, sol−gel methods have the potential to yield materials with better compositional homogeneity than those obtained with SSR due to molecular mixing of the precursors.[12] Furthermore, many sol−gel combustion type syntheses enable easy production of nanosized powders, which is attractive for the purpose of producing LLZO thin films[13,14] and to enable faster densification during sintering, often at lower temperatures.[15] Smaller grain sizes in LLZO may also yield particular benefits, such as reduced interfacial resistance between LLZO and lithium as well as decreased reaction with atmospheric carbon dioxide.[16] Finally, nanostructured LLZO appears to be particularly effective when used as an active filler to enhance the ionic conductivity of composite polymer electrolytes (CPEs),[17] as has been demonstrated using nanosized LLZO prepared via ball-milling,[18] hydrogel templating,[19] nanocellulose templating,[20] and electrospinning.[21,22]

The most common type of sol−gel synthesis employed for LLZO is based on the combustion of an organic fuel with metal nitrates as precursors and oxidizers.[4−6,11,17] The Pechini method, for example, relies on *in situ* polymerization between citric acid and ethylene glycol to form a combustible polymer, which has the effect of chelating metal ions by virtue of the presence of citric acid.[12,23] Heating to mild temperatures results in a reactive precursor, which yields fine oxide powders

Received: November 4, 2019
Accepted: December 4, 2019
Published: December 4, 2019






DOI: 10.1021/acsami.9b19981
ACS Appl. Mater. Interfaces 2020, 12, 953−962

after calcination. This combustion type sol−gel approach is distinct from more conventional sol−gel approaches wherein a metal oxide gel is obtained, such as in the method of Sakamoto et al.[8] A second class of combustion synthesis relies on a nanostructured sacrificial template to produce nanosized LLZO. For example, LLZO nanowires were demonstrated[22,24] via electrospinning polymer fibers containing a LLZO sol, followed by controlled combustion. A different approach uses cellulose nanofibers as template,[20,25] in which the sol is impregnated followed by calcination to obtain LLZO. A third combustion-related synthesis approach relies on spray pyrolysis, such as has been applied to ALLZO and GLLZO by using liquid feed flame spray pyrolysis.[13,14] While using similar metalorganic precursors as some other sol−gel type methods, this method uses combustion of an aerosol comprising a fuel-precursor mixture as the sole heat source and forms "decomposed LLZO", rather than LLZO, which must be subsequently calcined or sintered to obtain the crystalline product.[13,14]

While sol−gel type synthesis of LLZO based on solution combustion or templating has been successful in the aforementioned cases, there are some drawbacks. In the case of electrospinning, throughput of material tends to be a challenge, yielding typical production rates of tens of milligrams per hour unless an advanced electrospinning apparatus is used.[26,27] Use of a nanostructured sacrificial template such as nanocellulose fibers requires an unusual and costly material for templating, which is completely consumed in the process.[25] The reliance on an *in situ* polymerization process for Pechini-type combustion synthesis[12] may be a source of irreproducibility. In addition, these processes also generally rely on metal nitrate salts as precursors, which rapidly produce large amounts of excess heat during combustion, often limiting scalability (due to potential for runaway combustion/explosion[12]) and reducing reproducibility of the as-synthesized materials.[23] The liquid feed flame spray pyrolysis method requires specialty precursors (e.g., in-house synthesized alumatrane or gallium atrane, lanthanum and zirconium isobutyrate, and lithium propionate)[13,14] and a much more complex reactor than the method discussed in this work.

These issues of low throughput, irreproducibility, and complexity motivated adoption of a potentially more versatile combustion strategy, known as the "polymer sol−gel method" or simply the "polymer method". In this approach, a solution of metal precursors and a polymer are simply dissolved together, dried, and combusted to produce oxide powders.[12] This has the effect of homogeneously distributing precursors and forming a uniform "fuel" mixture in one step, unlike the aforementioned procedures. An aqueous polymer method for LLZO was recently reported using a poly(vinyl alcohol)-based hydrogel as matrix for the LLZO nitrate precursors.[19] Herein, a unique nonaqueous polymer (NAP) method is employed to synthesize nanopowders of LLZO. Additionally, two aqueous combustion synthesis methods, both based on metal nitrates but with different carbon sources, are described and contrasted to the nonaqueous method. In all cases, c-LLZO can be obtained at reasonably low temperatures between 700 and 800 °C. Ta-doped LLZO (LLZTO) nanopowders obtained from the NAP method are consolidated using simple pressureless sintering, demonstrating both high density and high ionic conductivity. Our results show that the NAP combustion route is a promising method to obtain LLZO nanopowder, which is more straightforward than other template-based combustion syntheses, less limited in terms of throughput, and allows more controllable combustion compared to conventional nitrate-based combustion methods.

## EXPERIMENTAL SECTION

The synthesis of LLZO using the nonaqueous polymer (NAP) method was performed using lanthanum, lithium, and zirconium acetylacetonate reagents ("acac") as precursors (and optionally tantalum(V) ethoxide as a dopant source). Propionic acid (PA), poly(vinylpyrrolidone) (PVP), and dichloromethane (DCM) were used as solvent, polymer, and cosolvent, respectively. For comparison, LLZO was also prepared from aqueous solutions using tannic acid (TA) or poly(vinyl alcohol) (PVA) and nitrate salt precursors. For brevity, the aqueous processes using PVA and TA are termed "PVA" and "TA". Combustion of the mixtures was performed in air between 600 and 800 °C. Pellets were prepared by conventional uniaxial pressing using as-synthesized calcined nanopowders or by mixing nanopowders with 5 wt % anhydrous LiOH. The pellets were embedded in mother powder as shown in Figure S1 and sintered at 1100 °C for 6−15 h or 1200 °C for 2−12 h. For preliminary characterization, pellets were contacted with graphite[28] electrodes, and ionic conductivity measurements were performed using electrochemical impedance spectroscopy at 25 °C. Subsequently, lithium electrodes comprising a 20 wt % (~1.5 mol %) Sn−Li alloy[29] were applied for temperature-dependent ionic conductivity measurements. More detailed descriptions of the experimental procedures can be found in the Supporting Information.

The general synthesis procedure for the nonaqueous polymer sol−gel method is outlined in Scheme 1, with the aqueous synthesis methods following a similar flow as described in the Supporting Information (Table S1). In both the aqueous and NAP methods, reagents are initially dissolved in a solvent system (water or PA with DCM) to result in molecular mixing of precursors. Then, an organic component (PVA, PVP, or TA) is added to serve as fuel and maintain homogeneous distribution of the precursors after solvent removal.

**Scheme 1. (Top) Synthesis Procedure for Nonaqueous Polymer Combustion Process for LLZO; (Bottom) Photograph of LLZO Powder in an Agate Mortar Showing Foamlike Morphology of the Powders after Calcination**

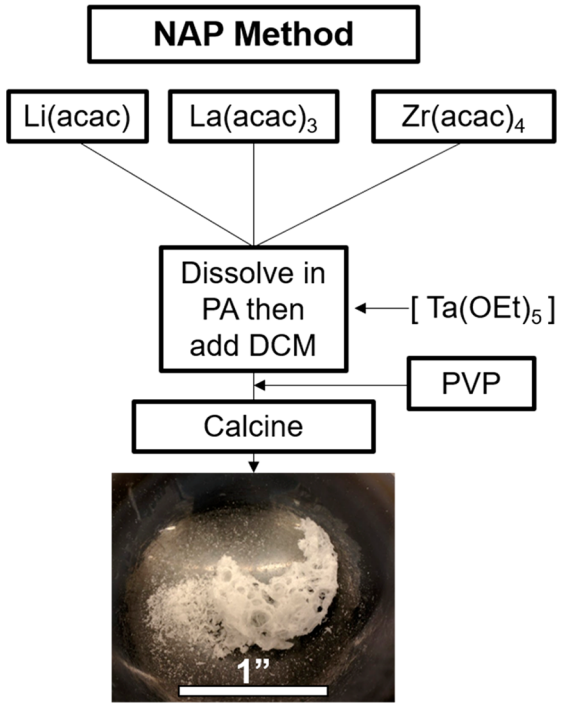




DOI: 10.1021/acsami.9b19981
ACS Appl. Mater. Interfaces 2020, 12, 953−962

Finally, the mixture (optionally predried) is calcined, which initially results in conversion of the organic material to a carbonized matrix, followed by complete burnout of the carbon and formation of oxide nanocrystals. In all three cases, under the correct calcination conditions, undoped c-LLZO is obtained.

## RESULTS AND DISCUSSION

**Synthesis of LLZO.** To elucidate the thermal decomposition process in the NAP method, a dried film of the precursor was characterized by thermogravimetric and differential thermal analysis (TGA/DTA) in air from room temperature (RT) to 800 °C (Figure 1). During heating

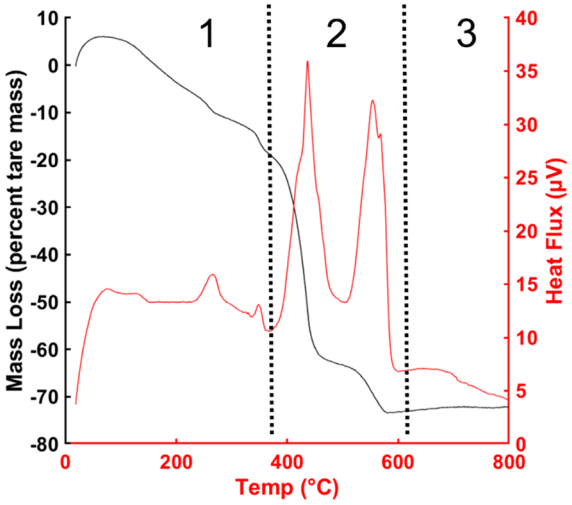


**Figure 1.** TGA/DTA analysis of dried NAP precursor, showing % mass loss (black) as a function of temperature and heat flux (red) coinciding with mass loss (exothermic processes pointing upward).

from RT to 400 °C (region 1), a slight mass increase was observed (most likely due to uptake of moisture or chemical addition of oxygen due to thermal oxidation of the polymer), followed by a steady mass loss with two small exothermic peaks. This most likely originates from the decomposition of organic ligands (i.e., acetylacetonate and propionate).[30] Region 2 is marked by a sharp mass loss beginning at around 400 °C with a brief plateau at 500 °C, followed by another sharp loss between 500 and 600 °C. The first exothermic process can be attributed to the oxidative decomposition of the pyrrolidone ($C_5H_9NO$) groups of the polymer with conversion of the remaining organic matter to carbon and the second exotherm to the complete thermal oxidation of the remaining carbon to $CO_2$.[31] Finally, region 3 is believed to correspond to the formation and growth of LLZO particles.

X-ray diffraction (XRD) patterns for a subset of synthesis conditions used to prepare undoped LLZO using the PVA, TA, and NAP methods are shown in Figure S2. In all three methods, $La_2Zr_2O_7$ (LZO) is observed for incomplete reactions, while the tetragonal phase (t-LLZO) begins to form when excessive calcination time is employed. This is in line with previous observations, where the cubic phase is observed in undoped LLZO nanowires, but extended calcination causes particle growth and concomitant appearance of t-LLZO.[24] Reducing the size of LLZO to nanometric dimensions has been demonstrated[24] to produce undoped cubic LLZO (c-LLZO, space group $Ia\bar{3}d$),[3] whereas the thermodynamically favorable but poorly conducting tetragonal phase (t-LLZO, space group $I4_1/acd$)[32] is formed in bulk LLZO in the absence of aliovalent dopants. This effect was also observed incidentally in several reports,[6,7,25,33] though not discussed in detail, and is hypothesized to originate from a size-stabilization effect of c-LLZO in undoped nanostructures.[24]

The calcination conditions and products for the NAP cases are summarized in Table 1, with corresponding XRD patterns

**Table 1. Summary of NAP Method Synthesis Conditions Leading to Incomplete and Complete Formation of Undoped c-LLZO**

| sample | hold temp (°C) | time (h) | result |
|---|---|---|---|
| NAP-1 | 700[a] | 2 | mixture of LZO and c-LLZO |
| NAP-2 | 700[a] | 4 | undoped c-LLZO |
| NAP-3 | 750[a] | 2 | mixture of c-LLZO and t-LLZO |
| NAP-4 | 800[b] | 0.5 | undoped c-LLZO |
| NAP-5 | 800[b] | 1 | mixture of c-LLZO and t-LLZO |

[a]Held at 400 °C for 2 h before final hold temperature. [b]2× heating rate compared to other samples, LZO = $La_2Zr_2O_7$.

in Figure S2. Based on the TGA/DTA analysis, for one set of experiments (NAP-1, NAP-2, and NAP-3), a 2 h hold at 400 °C was introduced to controllably carbonize but not completely burn away the organic components before ramping to the final hold temperature, since PVP converts to carbon in air at roughly 400 °C.[31] Pure-phase c-LLZO can be obtained after calcination for 4 h at 700 °C (after the 400 °C hold) or 0.5 h at 800 °C (no intermediate hold), but precise control over the reaction conditions is crucial for obtaining cubic LLZO without addition of extrinsic dopants.

While specific conditions required to obtain undoped c-LLZO differ somewhat between each of the three methods, all follow the same general progression, with c-LLZO observed under conditions at which nanosized powders are formed with minor to no impurity phases based on XRD analysis. Representative XRD patterns (Figure 2a), scanning electron microscopy (SEM) (Figure 2b–d), and transmission microscopy (TEM) images (Figure 2e–g) for c-LLZO powders prepared from these methods are shown in Figure 2. It should be reiterated that no extrinsic dopants were added to the precursor solutions, implicating a size dependency on the formation of c-LLZO as outlined previously. This is corroborated by the fact that in each of the micrographs in Figure 2 the majority of feature sizes observed are smaller than 1 $\mu$m, even though some sintering between primary particles is observed. In Figure 2f,g, a thin flakelike particle is seen, with a 3 nm thick amorphous surface layer, which corresponds to the $Li_2CO_3$ layer that is known[34,35] to form on LLZO upon exposure to air. The small thickness (~3 nm) of the surface $Li_2CO_3$ layer indicates that despite the large amount of organic components used in this synthesis procedure, the excess $CO_2$ formed as a result of their combustion does not have a deleterious effect in excess $Li_2CO_3$ formation.

It is worth noting that in the case of both the aqueous methods, drying the precursor at relatively low temperatures (130–150 °C) resulted in conversion of the dried precursor to a dark brown material that had evidently partially combusted. In fact, when temperatures above ~130 °C were used to dry the precursors, actual combustion was sometimes observed, most likely due to initial decomposition of some of the nitrates, initiating a self-propagating reaction that is well-known to occur in similar combustion-type syntheses.[12] Additionally, it was observed that the amount of precursor combusted in one


DOI: 10.1021/acsami.9b19981
ACS Appl. Mater. Interfaces 2020, 12, 953–962

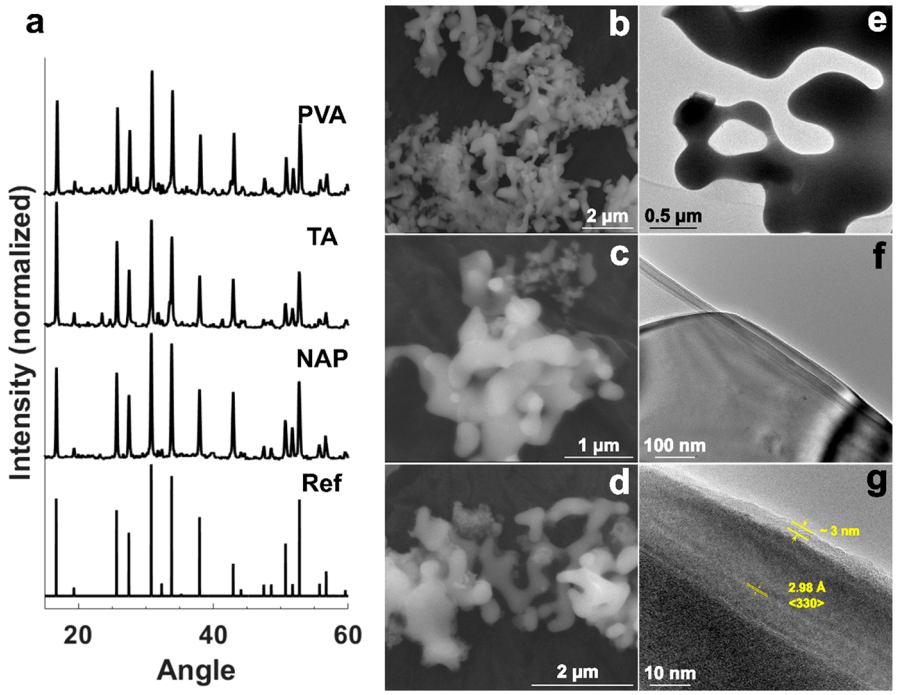


**Figure 2.** (a) XRD patterns corresponding to as-synthesized powders from the PVA, TA, and NAP methods, with c-LLZO reference (from Logéat et al.[36]); SEM images of powders from (b) PVA, (c) TA, and (d) NAP method. The calcination parameters used were 800 °C for 1.5 h for PVA, 700 °C for 1.5 h for TA, and 800 °C for 0.5 h for NAP. (e) TEM image of NAP ligament particles, (f) TEM image of flakelike NAP particle, and (g) HREM image of flakelike particle in (e) with ⟨330⟩ lattice fringes visible and ∼3 nm amorphous surface layer of $Li_2CO_3$.

synthesis run played a substantial role in the phase purity of the resultant material. For example, in one larger scale synthesis, once the onset of combustion occurred, the reaction was so energetic that it caused the furnace door to come open, most likely due to rapid evolution of gases. Such observations have been described elsewhere[23] as well. Clearly, the heat released during combustion of the organic material and metal nitrates can be expected to change the local temperature in the crucible due to a self-propagating combustion, distinct from the set temperature of the furnace.[23] This somewhat uncontrolled reaction may also be responsible for the noticeable impurity phases seen in the XRD patterns (Figure 2a) for material prepared from the PVA and TA methods. A similar issue was seen with nanocellulose templated LLZO by using the same type of nitrate precursors.[25]

However, this was less of a problem for the NAP method, which did not rely on highly reactive nitrates, and thus further investigations focused on material synthesized by this method. It should also be noted that a NAP process using acetic acid instead of PA was also attempted, but this resulted in hydrolysis of the sol in a matter of minutes after reagents were mixed. In contrast, use of PA resulted in highly stable sols that could be stored for several months in ambient atmosphere without observable precipitation or degradation. This is believed to arise from formation of propionate complexes, which are somewhat more hydrophobic than acetates and provide better steric hindrance against hydrolysis for the otherwise reactive metalorganic species (in particular, tantalum ethoxide) used.

**Synthesis and Formation Mechanism of LLZTO via the NAP Method.** Because grain coarsening of undoped c-LLZO causes its transformation to t-LLZO, Ta-doped LLZO (LLZTO) of nominal composition $Li_{6.4}La_3Zr_{1.4}Ta_{0.6}O_{12}$ was prepared via NAP (Supporting Information) to preserve the highly conductive cubic phase during pellet sintering. After minor optimization of the synthesis parameters, it was determined that phase-pure LLZTO could be obtained at 700 °C in 3.5 h, with the reaction time evidently decreased slightly by Ta-doping. This may be due to LLZTO being a more energetically favorable phase than c-LLZO, as corroborated by computational studies.[37] For preparation of larger batches of nanopowder, a direct ramp and 4 h hold at 700 °C was used to ensure that the excess of carbon was fully removed. Representative SEM images and an XRD pattern of LLZTO used in this study are shown in Figure 3, and an EDS map in Figure S3 indicates uniform distribution of the Ta dopant. These results show that the NAP method may be easily extended to include dopants while maintaining the same morphology and phase purity of undoped c-LLZO.

To more clearly understand the formation mechanism of nanosized particles via the polymer method, some of the LLZTO precursor solution was heated to 400 °C for 2 h in air to mimic the formation of the carbon material that is generated prior to formation of LLZTO. High-angle annular dark field (HAADF) scanning transmission electron microscopy (STEM) was performed on the partially combusted samples, with electron energy loss spectroscopy (EELS) and energy dispersive spectroscopy (EDS) spectral images acquired simultaneously and shown in Figure 4.

In the HAADF-STEM image in Figure 4a, a cluster of particles with high contrast can be seen embedded in a foamlike material with much lower contrast. This type of contrast difference in HAADF imaging is to be expected between a high atomic number (high-Z material) and a low-Z material, alluding to the presence of partially formed oxides dispersed within a carbon matrix. A higher magnification image in Figure 4a (inset) shows that at least some of the particles are evidently ensembles or aggregates of ultrafine particles. Figure


DOI: 10.1021/acsami.9b19981
ACS Appl. Mater. Interfaces 2020, 12, 953−962

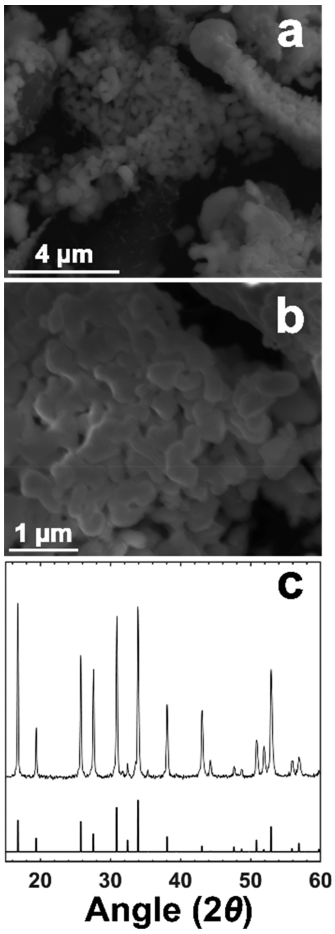


**Figure 3.** (a) Representative SEM image of as-synthesized LLZTO from the NAP method, (b) higher magnification image from (a), and (c) representative XRD pattern of as-synthesized LLZTO from the NAP method (ref 36).

4b shows another HAADF-STEM image corresponding to the spectral images in Figure 4c,d, with the region of interest outlined as a yellow box. To determine the identity of the materials, a STEM-EELS map (Figure 4c, example EELS spectrum in Figure S4) and a STEM-EDS map (Figure 4d) were simultaneously acquired, allowing for chemical imaging of carbon, zirconium, lanthanum, and tantalum. The blue regions in Figure 4c correspond to signal from the La-$M_{4,5}$ edge signal, which originates exclusively from the high-$Z$ contrast particles in Figure 4a. The C K-edge signal (yellow) originates from the surrounding matrix, confirming that during intermediate stages of combustion precursors begin to form nanosized particles within a foamy carbon matrix. This is further corroborated by the STEM-EDS map in Figure 4d, showing the coinciding signals from La, Zr, and Ta (blue, green, and red, respectively). An exception is one Ta-rich region (outlined with a yellow dotted line), which evidently appears as a separate phase as no La or Zr signals are observed. The signal from the N K-peak is markedly absent from the EDS spectra (Figure S5) of the carbon material shown in Figure 4, corroborating the assignment of the first exothermic peak in region 2 of Figure 1 as complete decomposition of PVP (i.e., removal of nitrogen-containing pyrrolidone groups) to form a pure carbon phase when the temperature is held at 400 °C.

The presence of oxide particles in this carbonaceous matrix indicates that the foam forms *in situ* and acts as a template that physically disperses and restricts contact and sintering between individual LLZO particles as they begin to form. The evolution of LLZO from the polymer sol−gel solution is shown schematically in Scheme 2, showing the uniform polymer sol converting to a transient carbon foam embedded with distributed oxide particles, and finally the resultant LLZO particle network. This process has some notable advantages over other similar templating methods. The ability to template LLZO without requiring premade fibers is one benefit to this polymer sol−gel method. In addition, the long-term stability of the precursor solution and ability to produce larger amounts of

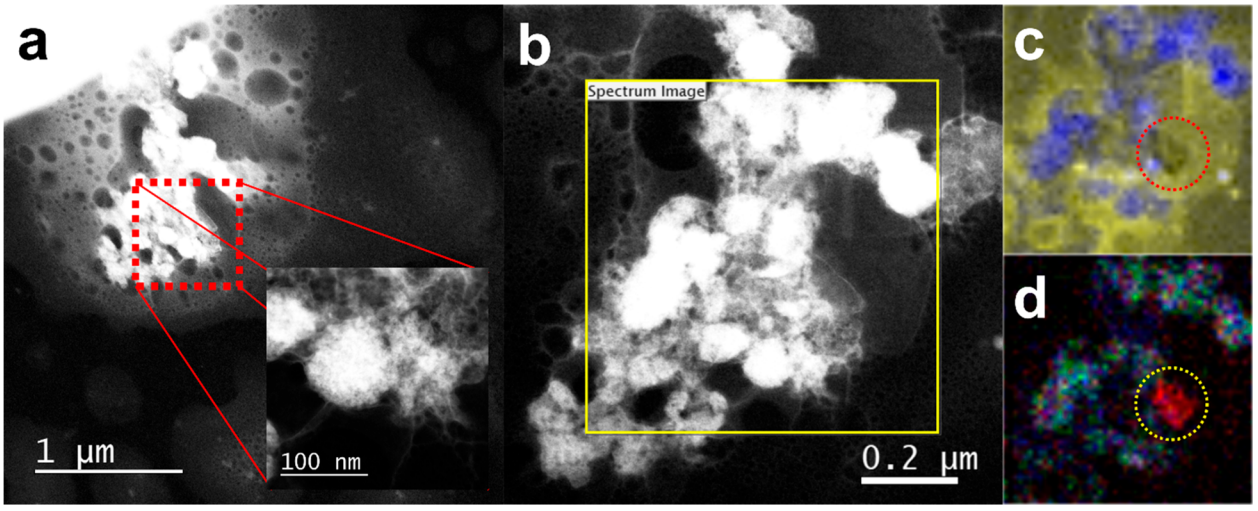


**Figure 4.** HAADF-STEM spectral image analysis of carbonized NAP precursor powder: (a) survey HAADF-STEM image (higher magnification image in inset), (b) HAADF-STEM image with region of interest shown as a yellow box, (c) STEM-EELS map of region of interest in (b) showing map of integrated C K-edge (284 eV) signal in yellow and La $M_{4,5}$-edges (849 and 832 eV, respectively) signal in blue, and (d) STEM-EDS map of region of interest in (b) showing map of integrated signal from the La L-peak (~4.65 keV) in blue, Ta M-peak (~1.7 keV) in red, and Zr L-peak (~2 keV) in green.



DOI: 10.1021/acsami.9b19981
ACS Appl. Mater. Interfaces 2020, 12, 953−962

**Scheme 2. Hypothesized Process of Formation of Nanosized LLZO from Polymer Sol–Gel Solutions with Corresponding Photographs of the As-Made Yellow Polymer Sol, Partially Combusted Oxidic Particles Embedded Inside Carbon Foam Matrix, and White LLZO Powders after Full Calcination**

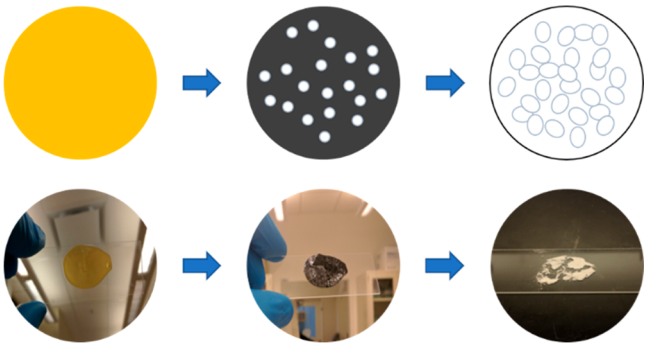

material in shorter times relative to templating methods are significant advantages.

**Densification and Ionic Conductivity Measurements.** Both undoped and Ta-doped LLZO powders prepared by using the NAP method were pressed and sintered at various temperatures for ionic conductivity measurements via electrochemical impedance spectroscopy (EIS). However, good impedance spectra for the undoped c-LLZO pellet could not be obtained due to the low pellet densities obtained at sintering temperatures (i.e., 600 °C) at which the cubic phase was maintained (see Figures S6 and S7). Sintering the undoped LLZO powder at 1100 °C caused the expected transformation to t-LLZO. LLZTO, however, was easily densified at 1100 and 1200 °C as can be seen from highly dense grain structures seen in SEM fracture surface images (Figure 5a,b). Ionic conductivity and relative density values from sintering at 1200 and 1100 °C for various times are shown in Figure 5c,d, respectively. Nyquist plots (Figure S8) were characterized by a single depressed partial semicircle, which is common for EIS measurements performed on LLZO pellets at room temperature. Representative XRD patterns of pellets sintered at 1100 and 1200 °C are shown in Figure S9. The addition of some excess lithium (5 wt % anhydrous LiOH) was employed before pressing and sintering the LLZTO pellets at 1200 °C under mother powder to offset the volatilization of lithium at high temperature, which is known to result in low ionic conductivity or decomposition of the LLZO lattice.[33,38] LiOH was chosen over $Li_2CO_3$ as it melts at a lower temperature and was thus expected to uniformly wet the LLZTO powder and thus more uniformly offset Li volatilization.

On the basis of measured ionic conductivity and density results from pellets sintered at 1200 °C (Figure 5a,c), it can be seen that the highest pellet density and ionic conductivity do not occur under the same sintering conditions and that

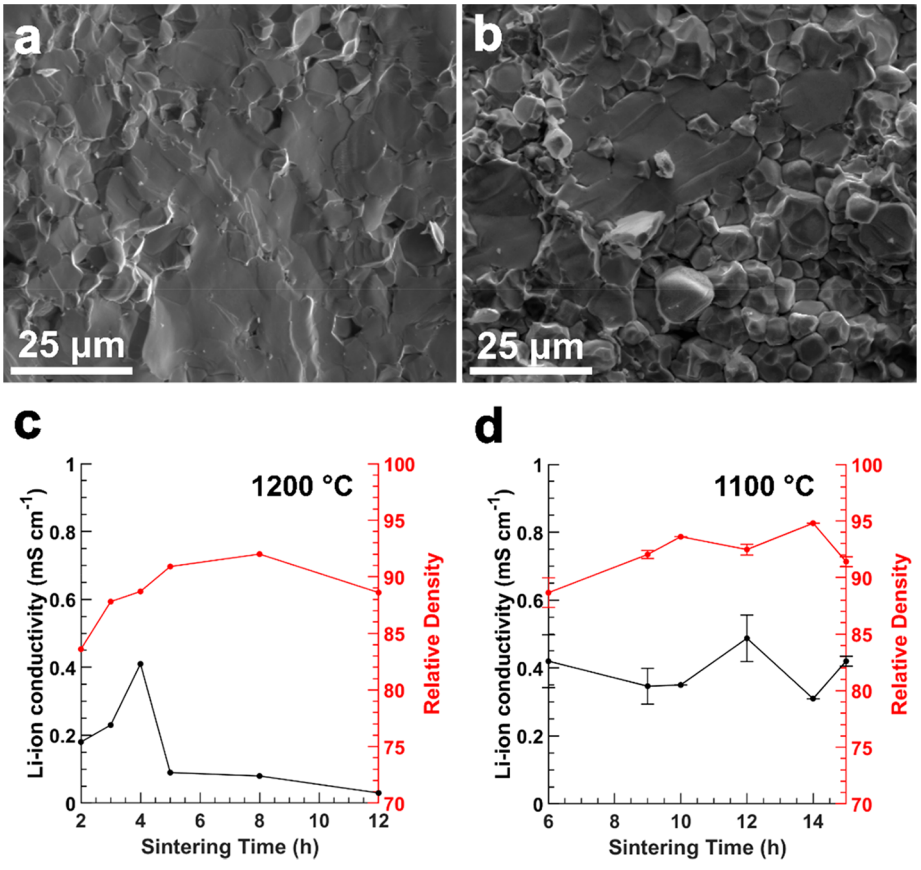


**Figure 5.** (a) SEM fracture surface image of a pellet sintered at 1200 °C, (b) SEM fracture surface image of a pellet sintered at 1100 °C, (c) total ionic conductivity and relative density of pellets sintered at 1200 °C for 2–12 h, and (d) total ionic conductivity and relative density of pellets sintered at 1100 °C for 6–15 h (average values of conductivity and density from multiple pellets sintered at 6, 9, 12, and 15 h with error bars equal to the standard deviation).



DOI: 10.1021/acsami.9b19981
ACS Appl. Mater. Interfaces 2020, 12, 953–962

reasonably high ionic conductivity only occurs for one sintering condition (4 h). This indicates that despite the added LiOH and mother powder covering the pellets, Li loss likely results in lower ionic conductivity for sintering conditions that provide high density. Huang et al. recently reported the importance of maintaining a $Li_2O$-rich vapor phase during sintering of LLZO to obtain high densities and ionic conductivity.[39] From our results, it appears that simple addition of LiOH to pellets and use of mother powder is insufficient for sintering at 1200 °C. Loss of Li at high temperatures may also induce oxygen vacancy formation, which can also lower the conductivity in Ta-doped LLZO.[40] In another case, a small increase in Li content of 4% in LLZO was also reported to result in 120% increase in ionic conductivity,[41] which implies conversely that sintering for slightly too long may result in enough deviation from optimal Li content through Li volatility to drastically reduce conductivity. Finally, it was shown in studies of Li diffusion by muon-spin relaxation and quasi-elastic neutron scattering that the number of mobile $Li^+$ species is the primary factor determining ionic conductivity in garnets,[42] indicating that Li loss that is not severe enough to decompose[38] LLZO outright may still drastically lower ionic conductivity.

Therefore, to minimize the negative effects of Li volatility, pellets were also sintered at a lower temperature of 1100 °C for slightly longer times in smaller volume MgO crucibles (a photograph of this setup can be found in Figure S1b). In this case, rather than addition of excess LiOH to the powder, the LLZTO nanopowder was pressed as-synthesized and covered with a mixture containing mother powder and $Li_2O_2$, which decomposes to form $Li_2O$ beginning at ~250 °C.[43] By providing excess $Li_2O$ and utilizing a lower sintering temperature, higher ionic conductivities and higher relative densities were achieved over a wide range of sintering times. The fact that this LLZTO powder is nanosized likely also plays a role[15] in allowing high densities to be achieved via pressureless sintering at the relatively low temperature of 1100 °C. Similarly high densities were also reported at low sintering temperatures for flame-spray pyrolysis LLZO nanopowders.[13,14] Multiple pellets were sintered for 6, 9, 12, and 15 h at 1100 °C to assess replicability, with results (minima and maxima of conductivity and density) presented in Table S2. Ionic conductivity and density values for pellets sintered at 1100 °C are plotted in Figure 5d (with averaged values from multiple pellets shown for 6, 9, 12, and 15 h sintering times). Pellets sintered at 1200 and 1100 °C both exhibit transgranular fracture, indicating strong grain cohesion, although the samples sintered at 1100 °C display intergranular fracture as well (Figure 5b).

The temperature dependence of ionic conductivity was investigated for some of the pellets sintered at 1100 °C to determine the activation energy and was calculated by performing EIS measurements at several temperatures between 25 and 70 °C and taking a linear fit of $\ln(\sigma)$ (S $cm^{-1}$) vs $1/T$ ($K^{-1}$). EIS spectra used for these calculations are shown in Figure 6, with the resultant Arrhenius plots shown in Figure S10. Based on the slopes of the linear fits, the activation energies for these LLZTO pellets vary between 0.34 and 0.42 eV, corresponding well to other values in the literature (see Table 2).

Table 2 contains a comparison of various synthesis methods targeting nanosized LLZO based on sol–gel, combustion, and other novel synthetic methods from the literature, with

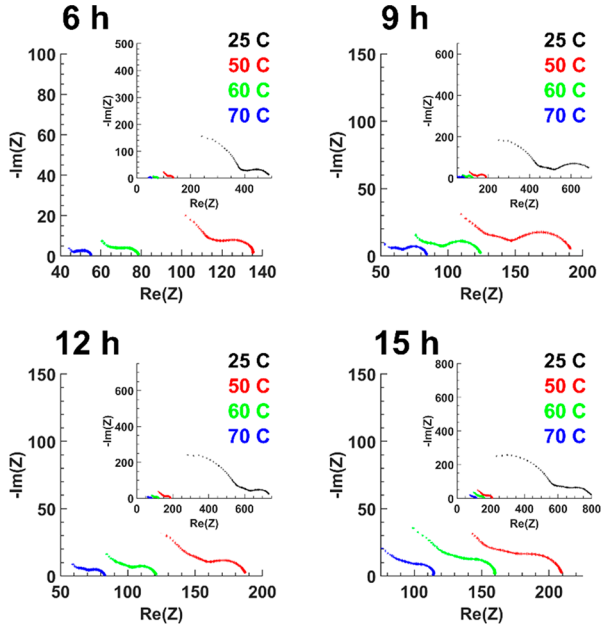


**Figure 6.** Temperature-dependent EIS spectra of LLZTO pellets sintered at 1100 °C for 6, 9, 12, and 15 h.

synthesis conditions and performance metrics for comparison to the NAP method. From these results, it is evident that the NAP method can yield nanopowders that result in high ionic conductivity comparable to or surpassing other methods by simple pressureless sintering in air, which could be improved further with optimization of the pellet sintering process or use of advanced sintering techniques such as hot pressing. Additionally, the use of a lower sintering temperature and $Li_2O_2$ to increase the $Li_2O$ vapor pressure during sintering allows for high density and conductivity to be obtained over a wide range of sintering times, even at a relatively short sintering time of 6 h, while also reducing the amount of mother powder needed. The small particle size of the LLZTO nanopowder likely also contributes to higher density at this lower sintering temperature. These benefits along with the observation that the NAP method enables greater control over combustion conditions compared to the conventional nitrate-based methods outlined above make this a promising synthetic approach for obtaining LLZO nanopowders of potentially many compositions, allowing lower synthesis and sintering temperatures of garnet solid electrolytes.

## CONCLUSIONS

In summary, a novel combustion synthesis route to obtain nanosized LLZO is presented. Three distinct synthesis methods were employed to investigate the effect of the type of metal precursor, solvent system, and organic fuel. Both aqueous methods using metal nitrate precursors were effective for preparing LLZO but demonstrated a strong propensity towards runaway combustion, which is commonly observed in such combustion syntheses. On the other hand, the non-aqueous method using metalorganic precursors ameliorated this issue, enabling relatively better reproducibility and control over synthesis conditions. The combination of molecular mixing of precursors throughout an organic medium synergizes with the formation of a carbonaceous foam during intermediate stages of combustion, which acts as an *in situ* sacrificial template, with the effect of segregating pockets of


DOI: 10.1021/acsami.9b19981
ACS Appl. Mater. Interfaces 2020, 12, 953–962

Table 2. Comparison of Sol−Gel, Combustion, and Coprecipitation Type Synthesis Methods for Al-Doped (ALLZO), Ga-Doped (GLLZO), and Ta-Doped ($Li_{6.4}La_3Zr_{1.4}Ta_{0.6}O_{12}$ Unless Noted, LLZTO) LLZO from Various Works in the Literature

| | | synthesis conditions | | pellet sintering conditions | | sintered pellet properties | | | |
|---|---|---|---|---|---|---|---|---|---|
| type of LLZO | synthesis technique | time (h) | temp (°C) | time (h) | temp (°C) | density (%) | RT total ionic conductivity (mS $cm^{-1}$) | activation energy (eV) | reference |
| ALLZO | sol−gel | 4 | 600−800 | 1 | 1000 | 96 | 0.40[b] | 0.41 | Sakamoto et al.[8] |
| ALLZO | coprecipitation | 10 | 850 | 20 | 1150 | >90 | 0.20 | 0.25 | Shao et al.[44] |
| ALLZO | coprecipitation | 6 | 850 | 1 | 1000 | 57 | 0.06[c] | 0.58 | Langer et al.[45] |
| ALLZO | nitrate−glycine combustion | 6 | 750 | 6 | 1200 | 95 | 0.51[d] | 0.29 | Dhivya et al.[46] |
| ALLZO | coprecipitation | 6 | 900 | 0.05 | 1000 | 96.5 | 0.33[e] | 0.32 | Zhang et al.[47] |
| ALLZO | flame-spray pyrolysis | N/A | N/A | 1 | 1080 | 94 | 0.2 | 0.35 | Yi et al.[13] |
| GLLZO | flame-spray pyrolysis | N/A[a] | N/A | 0.3 | 1130 | 95 | 1.3 | 0.28 | Yi et al.[14] |
| GLLZO | nitrate combustion | 10−15 | 650 | 6 | 950 | 76 | 0.24 | 0.32 | Afyon et al.[11] |
| LLZTO | coprecipitation | 8 | 750 | 6 | 1125 | NR[a] | 0.20 | NR | Chen et al.[48] |
| LLZTO | sol−gel | 2 | 900 | 0.33 | 1000 | 88 | 0.05[b] | 0.43 | El-Shinawi et al.[49] |
| LLZTO | sol−gel[g] | 12 | 900 | 36 | 1180 | 96 | 0.45 | 0.529 | Ishiguro et al.[50] |
| LLZTO | sol−gel[f] | 4 | 950 | 4 | 1100 | NR | 0.21 | NR | Yoon et al.[51] |
| LLZTO | sol−gel[f] | 4 | 900 | 1 | 1100 | 92 | 0.48[b] | NR | Kim et al.[52] |
| LLZTO | NAP method | 4 | 700 | 6−15 | 1100 | 90.5−93.6 | 0.24−0.67 | 0.34−0.42 | this work |

[a]NR = not reported; N/A = not applicable. [b]Consolidated by using hot-pressing. [c]Measured at 80 °C. [d]Measured at 30 °C. [e]Consolidated by using field-assisted sintering. [f]$Li_{6.5}La_3Zr_{1.5}Ta_{0.5}O_{12}$. [g]$Li_{6.3}La_3Zr_{1.3}Ta_{0.7}O_{12}$.

reagents throughout, thus physically restricting particle size growth as the oxides are forming. Elucidation of the formation of this transient carbonaceous foam was performed via electron microscopy and illustrates the mechanism by which this combustion synthesis results in nanosized LLZO. All three methods enabled formation of nanosized, undoped c-LLZO under the correct calcination conditions. Ta-doped LLZO was also easily synthesized by the nonaqueous route, demonstrating high total ionic conductivity of 0.24−0.67 mS $cm^{-1}$ after simple pressureless sintering at 1100 °C in air for between 6 and 15 h, with an activation energy of 0.34−0.42 eV. The polymer combustion route described herein is a promising alternative synthesis route to controlled preparation of nanosized LLZO, utilizing less reactive reagents and demonstrating lower complexity compared to many other synthesis routes targeting nanosized LLZO.

## ■ ASSOCIATED CONTENT

### Supporting Information

The Supporting Information is available free of charge at https://pubs.acs.org/doi/10.1021/acsami.9b19981.

Experimental procedures for synthesis and characterization, tabulated pellet data and electrochemical data, description of data processing for EELS and EDS spectra for STEM spectral imaging, XRD patterns, and SEM images (PDF)

## ■ AUTHOR INFORMATION


### Corresponding Author

*E-mail: candace.chan@asu.edu.

### ORCID

J. Mark Weller: 0000-0003-2056-8974

Candace K. Chan: 0000-0003-4329-4865


### Notes

The authors declare no competing financial interest.

## ■ ACKNOWLEDGMENTS

This work was supported by the NSF CAREER Award DMR 1553519, an ASU Fulton Schools of Engineering Dean's Fellowship (J.M.W.), and the Fulton Undergraduate Research Initiative (J.A.W.). The authors gratefully acknowledge the use of facilities within the LeRoy Eyring Center for Solid State Science, the Goldwater Materials Science Facility, and the John M. Cowley Center for High Resolution Electron Microscopy at Arizona State University. J.M.W. thanks Dr. Barnaby Levin for helpful discussions regarding processing and interpretation of EDS and EELS data.

## ■ REFERENCES


(1) Thangadurai, V.; Narayanan, S.; Pinzaru, D. Garnet-Type Solid-State Fast Li Ion Conductors for Li Batteries: Critical Review. *Chem. Soc. Rev.* **2014**, *43* (13), 4714−4727.

(2) Ramakumar, S.; Deviannapoorani, C.; Dhivya, L.; Shankar, L. S.; Murugan, R. Lithium Garnets: Synthesis, Structure, $Li^+$ Conductivity, $Li^+$ Dynamics and Applications. *Prog. Mater. Sci.* **2017**, *88*, 325−411.

(3) Murugan, R.; Thangadurai, V.; Weppner, W. Fast Lithium Ion Conduction in Garnet-Type $Li_7La_3Zr_2O_{12}$. *Angew. Chem., Int. Ed.* **2007**, *46* (41), 7778−7781.

(4) Shimonishi, Y.; Toda, A.; Zhang, T.; Hirano, A.; Imanishi, N.; Yamamoto, O.; Takeda, Y. Synthesis of Garnet-Type $Li_{7-X}La_3Zr_2O_{12-1/2x}$ and Its Stability in Aqueous Solutions. *Solid State Ionics* **2011**, *183* (1), 48−53.

(5) Janani, N.; Ramakumar, S.; Dhivya, L.; Deviannapoorani, C.; Saranya, K.; Murugan, R. Synthesis of Cubic $Li_7La_3Zr_2O_{12}$ by Modified Sol-Gel Process. *Ionics* **2011**, *17* (7), 575−580.

(6) Kokal, I.; Somer, M.; Notten, P. H. L.; Hintzen, H. T. Sol−Gel Synthesis and Lithium Ion Conductivity of $Li_7La_3Zr_2O_{12}$ with Garnet-Related Type Structure. *Solid State Ionics* **2011**, *185*, 42−46.

(7) Xie, H.; Li, Y.; Goodenough, J. B. Low-Temperature Synthesis of $Li_7La_3Zr_2O_{12}$ with Cubic Garnet-Type Structure. *Mater. Res. Bull.* **2012**, *47*, 1229−1232.

(8) Sakamoto, J.; Rangasamy, E.; Kim, H.; Kim, Y.; Wolfenstine, J. Synthesis of Nano-Scale Fast Ion Conducting Cubic $Li_7La_3Zr_2O_{12}$. *Nanotechnology* **2013**, *24* (42), 424005.




DOI: 10.1021/acsami.9b19981
ACS Appl. Mater. Interfaces 2020, 12, 953−962

(9) Kotobuki, M.; Kanamura, K.; Sato, Y.; Yamamoto, K.; Yoshida, T. Electrochemical Properties of $Li_7La_3Zr_2O_{12}$ Solid Electrolyte Prepared in Argon Atmosphere. *J. Power Sources* **2012**, *199* (24), 346−349.
(10) Bitzer, M.; Van Gestel, T.; Uhlenbruck, S.; Hans-Peter-Buchkremer. Sol-Gel Synthesis of Thin Solid $Li_7La_3Zr_2O_{12}$ Electrolyte Films for Li-Ion Batteries. *Thin Solid Films* **2016**, *615*, 128−134.
(11) Afyon, S.; Krumeich, F.; Rupp, J. L. M. A Shortcut to Garnet-Type Fast Li-Ion Conductors for All-Solid State Batteries. *J. Mater. Chem. A* **2015**, *3* (36), 18636−18648.
(12) Danks, A. E.; Hall, S. R.; Schnepp, Z. The Evolution of 'Sol−Gel' Chemistry as a Technique for Materials Synthesis. *Mater. Horiz.* **2016**, *3*, 91−112.
(13) Yi, E.; Wang, W.; Kieffer, J.; Laine, R. M. Flame Made Nanoparticles Permit Processing of Dense, Flexible, Li + Conducting Ceramic Electrolyte Thin Films of Cubic-$Li_7La_3Zr_2O_{12}$ (c-LLZO). *J. Mater. Chem. A* **2016**, *4*, 12947−12954.
(14) Yi, E.; Wang, W.; Kieffer, J.; Laine, R. M. Key Parameters Governing the Densification of Cubic-$Li_7La_3Zr_2O_{12}$ $Li^+$ Conductors. *J. Power Sources* **2017**, *352*, 156−164.
(15) Fang, Z. Z.; Wang, H.; Wang, X.; Kumar, V. Grain Growth during Sintering of Nanosized Particles. *Ceram. Trans.* **2010**, *209*, 389−400.
(16) Cheng, L.; Chen, W.; Kunz, M.; Persson, K.; Tamura, N.; Chen, G.; Doeff, M. Effect of Surface Microstructure on Electrochemical Performance of Garnet Solid Electrolytes. *ACS Appl. Mater. Interfaces* **2015**, *7* (3), 2073−2081.
(17) Chan, C. K.; Yang, T.; Mark Weller, J. Nanostructured Garnet-Type $Li_7La_3Zr_2O_{12}$: Synthesis, Properties, and Opportunities as Electrolytes for Li-Ion Batteries. *Electrochim. Acta* **2017**, *253*, 268−280.
(18) Zhang, J.; Zhao, N.; Zhang, M.; Li, Y.; Chu, P. K.; Guo, X.; Di, Z.; Wang, X.; Li, H. Flexible and Ion-Conducting Membrane Electrolytes for Solid-State Lithium Batteries: Dispersion of Garnet Nanoparticles in Insulating Polyethylene Oxide. *Nano Energy* **2016**, *28*, 447−454.
(19) Bae, J.; Li, Y.; Zhao, F.; Zhou, X.; Ding, Y.; Yu, G. Designing 3D Nanostructured Garnet Frameworks for Enhancing Ionic Conductivity and Flexibility in Composite Polymer Electrolytes for Lithium Batteries. *Energy Storage Mater.* **2018**, *15*, 46−52.
(20) Xie, H.; Yang, C.; Fu, K. K.; Yao, Y.; Jiang, F.; Hitz, E.; Liu, B.; Wang, S.; Hu, L. Flexible, Scalable, and Highly Conductive Garnet-Polymer Solid Electrolyte Templated by Bacterial Cellulose. *Adv. Energy Mater.* **2018**, *8* (18), 1703474.
(21) Yang, T.; Zheng, J.; Cheng, Q.; Hu, Y. Y.; Chan, C. K. Composite Polymer Electrolytes with $Li_7La_3Zr_2O_{12}$ Garnet-Type Nanowires as Ceramic Fillers: Mechanism of Conductivity Enhancement and Role of Doping and Morphology. *ACS Appl. Mater. Interfaces* **2017**, *9* (26), 21773−21780.
(22) Fu, K. K.; Gong, Y.; Dai, J.; Gong, A.; Han, X.; Yao, Y.; Wang, C.; Wang, Y.; Chen, Y.; Yan, C.; Li, Y.; Wachsman, E. D.; Hu, L. Flexible, Solid-State, Ion-Conducting Membrane with 3D Garnet Nanofiber Networks for Lithium Batteries. *Proc. Natl. Acad. Sci. U. S. A.* **2016**, *113* (26), 7094−7099.
(23) Wen, W.; Wu, J. M. Nanomaterials via Solution Combustion Synthesis: A Step Nearer to Controllability. *RSC Adv.* **2014**, *4* (101), 58090−58100.
(24) Yang, T.; Gordon, Z. D.; Li, Y.; Chan, C. K. Nanostructured Garnet-Type Solid Electrolytes for Lithium Batteries: Electrospinning Synthesis of $Li_7La_3Zr_2O_{12}$ Nanowires and Particle Size-Dependent Phase Transformation. *J. Phys. Chem. C* **2015**, *119* (27), 14947−14953.
(25) Gordon, Z. D.; Yang, T.; Morgado, G. B. G.; Chan, C. K. Preparation of Nano- and Microstructured Garnet $Li_7La_3Zr_2O_{12}$ Solid Electrolytes for Li-Ion Batteries via Cellulose Templating. *ACS Sustainable Chem. Eng.* **2016**, *4* (12), 6391−6398.
(26) Persano, L.; Camposeo, A.; Tekmen, C.; Pisignano, D. Industrial Upscaling of Electrospinning and Applications of Polymer Nanofibers: A Review. *Macromol. Mater. Eng.* **2013**, *298* (5), 504−520.
(27) Rosenthal, T.; Weller, J. M.; Chan, C. K. Needleless Electrospinning for High Throughput Production of $Li_7La_3Zr_2O_{12}$ Solid Electrolyte Nanofibers. *Ind. Eng. Chem. Res.* **2019**, *58* (37), 17399−17405.
(28) Shao, Y.; Wang, H.; Gong, Z.; Wang, D.; Zheng, B.; Zhu, J.; Lu, Y.; Hu, Y.-S.; Guo, X.; Li, H.; Huang, X.; Yang, Y.; Nan, C.-W.; Chen, L. Drawing a Soft Interface: An Effective Interfacial Modification Strategy for Garnet-Type Solid-State Li Batteries. *ACS Energy Lett.* **2018**, *3* (6), 1212−1218.
(29) Wang, C.; Xie, H.; Zhang, L.; Gong, Y.; Pastel, G.; Dai, J.; Liu, B.; Wachsman, E. D.; Hu, L. Universal Soldering of Lithium and Sodium Alloys on Various Substrates for Batteries. *Adv. Energy Mater.* **2018**, *8* (6), 1701963.
(30) Petit, S.; Morlens, S.; Yu, Z.; Luneau, D.; Pilet, G.; Soubeyroux, J. L.; Odier, P. Synthesis and Thermal Decomposition of a Novel Zirconium Acetato-Propionate Cluster: [Zr12]. *Solid State Sci.* **2011**, *13* (3), 665−670.
(31) Kozuka, H.; Takenaka, S. Single-Step Deposition of Gel-Derived Lead Zirconate Titanate Films: Critical Thickness and Gel Film to Ceramic Film Conversion. *J. Am. Ceram. Soc.* **2002**, *85* (11), 2696−2702.
(32) Awaka, J.; Kijima, N.; Hayakawa, H.; Akimoto, J. Synthesis and Structure Analysis of Tetragonal $Li_7La_3Zr_2O_{12}$ with the Garnet-Related Type Structure. *J. Solid State Chem.* **2009**, *182* (8), 2046−2052.
(33) Weller, J. M.; Whetten, J. A.; Chan, C. K. Synthesis of Fine Cubic $Li_7La_3Zr_2O_{12}$ Powders in Molten LiCl-KCl Eutectic and Facile Densification by Reversal of $Li^+/H^+$ Exchange. *ACS Appl. Energy Mater.* **2018**, *1* (2), 552−560.
(34) Cheng, L.; Liu, M.; Mehta, A.; Xin, H. L.; Lin, F.; Persson, K. A.; Chen, G.; Crumlin, E. J.; Doeff, M. M. Garnet Electrolyte Surface Degradation and Recovery. *ACS Appl. Energy Mater.* **2018**, *1* (12), 7244−7252.
(35) Larraz, G.; Orera, A.; Sanjuán, M. L. Cubic Phases of Garnet-Type $Li_7La_3Zr_2O_{12}$: The Role of Hydration. *J. Mater. Chem. A* **2013**, *1* (37), 11419−11428.
(36) Logéat, A.; Köhler, T.; Eisele, U.; Stiaszny, B.; Harzer, A.; Tovar, M.; Senyshyn, A.; Ehrenberg, H.; Kozinsky, B. From Order to Disorder: The Structure of Lithium-Conducting Garnets $Li_{7-x}La_3Ta_xZr_{2-x}O_{12}$ (X = 0−2). *Solid State Ionics* **2012**, *206*, 33−38.
(37) Miara, L. J.; Ong, S. P.; Mo, Y.; Richards, W. D.; Park, Y.; Lee, J. M.; Lee, H. S.; Ceder, G. Effect of Rb and Ta Doping on the Ionic Conductivity and Stability of the Garnet $Li_{7+2x-y}(La_{3-x}Rb_x)(Zr_{2-y}Ta_y)O_{12}$ ($0 \le x \le 0.375$, $0 \le y \le 1$) Superionic Conductor: A First Principles Investigation. *Chem. Mater.* **2013**, *25* (15), 3048−3055.
(38) Rangasamy, E.; Wolfenstine, J.; Sakamoto, J. The Role of Al and Li Concentration on the Formation of Cubic Garnet Solid Electrolyte of Nominal Composition $Li_7La_3Zr_2O_{12}$. *Solid State Ionics* **2012**, *206*, 28−32.
(39) Huang, X.; Lu, Y.; Song, Z.; Rui, K.; Wang, Q.; Xiu, T.; Badding, M. E.; Wen, Z. Manipulating Li2O Atmosphere for Sintering Dense $Li_7La_3Zr_2O_{12}$ Solid Electrolyte. *Energy Storage Mater.* **2019**, *22*, 207−217.
(40) Kubicek, M.; Wachter-Welzl, A.; Rettenwander, D.; Wagner, R.; Berendts, S.; Uecker, R.; Amthauer, G.; Hutter, H.; Fleig, J. Oxygen Vacancies in Fast Lithium-Ion Conducting Garnets. *Chem. Mater.* **2017**, *29* (17), 7189−7196.
(41) Thompson, T.; Sharafi, A.; Johannes, M. D.; Huq, A.; Allen, J. L.; Wolfenstine, J.; Sakamoto, J. A Tale of Two Sites: On Defining the Carrier Concentration in Garnet-Based Ionic Conductors for Advanced Li Batteries. *Adv. Energy Mater.* **2015**, *5* (11), 1500096.
(42) Nozaki, H.; Harada, M.; Ohta, S.; Watanabe, I.; Miyake, Y.; Ikedo, Y.; Jalarvo, N. H.; Mamontov, E.; Sugiyama, J. Li Diffusive Behavior of Garnet-Type Oxides Studied by Muon-Spin Relaxation and QENS. *Solid State Ionics* **2014**, *262*, 585−588.
(43) Yao, K. P. C.; Kwabi, D. G.; Quinlan, R. A.; Mansour, A. N.; Grimaud, A.; Lee, Y.; Lu, Y.; Shao-horn, Y. Thermal Stability of $Li_2O_2$


DOI: 10.1021/acsami.9b19981
*ACS Appl. Mater. Interfaces* 2020, 12, 953−962

and $Li_2O$ for Li-Air Batteries : In Situ XRD and XPS Studies. *J. Electrochem. Soc.* **2013**, *160* (6), 824−831.
(44) Shao, C.; Liu, H.; Yu, Z.; Zheng, Z.; Sun, N.; Diao, C. Structure and Ionic Conductivity of Cubic $Li_7La_3Zr_2O_{12}$ Solid Electrolyte Prepared by Chemical Co-Precipitation Method. *Solid State Ionics* **2016**, *287*, 13−16.
(45) Langer, F.; Glenneberg, J.; Bardenhagen, I.; Kun, R. Synthesis of Single Phase Cubic Al-Substituted $Li_7La_3Zr_2O_{12}$ by Solid State Lithiation of Mixed Hydroxides. *J. Alloys Compd.* **2015**, *645*, 64−69.
(46) Dhivya, L.; Karthik, S.; Ramakumar, S.; Murugan, R. Facile Synthesis of High Lithium Ion Conductive Cubic Phase Lithium Garnets for Electrochemical Energy Storage Devices. *RSC Adv.* **2015**, *5* (116), 96042−96051.
(47) Zhang, Y.; Cai, J.; Chen, F.; Tu, R.; Shen, Q.; Zhang, X.; Zhang, L. Preparation of Cubic $Li_7La_3Zr_2O_{12}$ Solid Electrolyte Using a Nano-Sized Core-Shell Structured Precursor. *J. Alloys Compd.* **2015**, *644*, 793−798.
(48) Chen, X.; Cao, T.; Xue, M.; Lv, H.; Li, B.; Zhang, C. Improved Room Temperature Ionic Conductivity of Ta and Ca Doped $Li_7La_3Zr_2O_{12}$ via a Modified Solution Method. *Solid State Ionics* **2018**, *314*, 92−97.
(49) El-Shinawi, H.; Cussen, E. J.; Corr, S. A. Enhancement of the Lithium Ion Conductivity of Ta-Doped $Li_7La_3Zr_2O_{12}$ by Incorporation of Calcium. *Dalton Trans.* **2017**, *46*, 9415−9419.
(50) Ishiguro, K.; Nemori, H.; Sunahiro, S.; Nakata, Y.; Sudo, R.; Matsui, M.; Takeda, Y.; Yamamoto, O.; Imanishi, N. Ta-Doped $Li_7La_3Zr_2O_{12}$ for Water-Stable Lithium Electrode of Lithium-Air Batteries. *J. Electrochem. Soc.* **2014**, *161* (5), A668−A674.
(51) Yoon, S. A.; Oh, N. R.; Yoo, A. R.; Lee, H. G.; Lee, H. C. Preparation and Characterization of Ta-Substituted $Li_7La_3Zr_{2-x}O_{12}$ Garnet Solid Electrolyte by Sol-Gel Processing. *Han'guk Seramik Hakhoechi* **2017**, *54* (4), 278−284.
(52) Kim, Y.; Yoo, A.; Schmidt, R.; Sharafi, A.; Lee, H.; Wolfenstine, J.; Sakamoto, J. Electrochemical Stability of $Li_{6.5}La_3Zr_{1.5}M_{0.5}O_{12}$ (M = Nb or Ta) against Metallic Lithium. *Front. Energy Res.* **2016**, *4*, 1−7.


DOI: 10.1021/acsami.9b19981
*ACS Appl. Mater. Interfaces* 2020, 12, 953−962